

# Conveyor belt X-ray CT using Domain Constrained Discrete Tomography

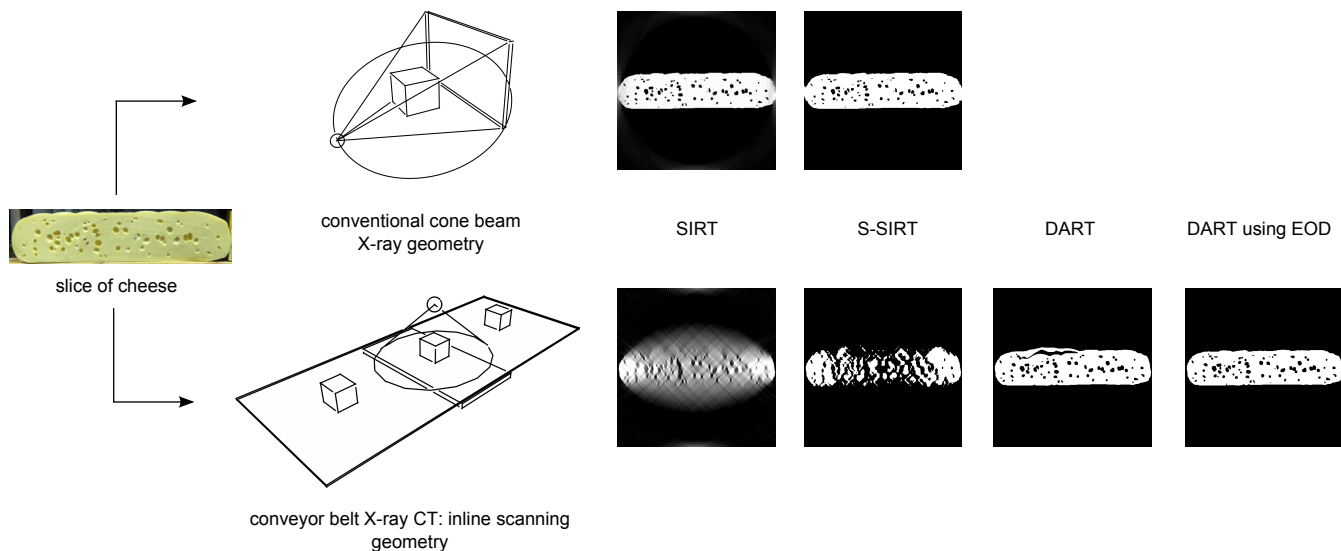


Fig. 1. CT reconstructions of a slice of cheese using conventional and inline scanning geometries. Due to the angular imaging constraints, the low number of available projections and the existence of truncated data, the reconstruction results in the inline geometry using conventional reconstruction algorithms (SIRT) are not acceptable. Those results can be improved by adding prior knowledge related to the expected density of the material (DART), and also prior knowledge related to the expected shape of the object, *i.e.*, considering only the values within a specific Expected Object Domain (EOD) during the reconstruction.

**Abstract**—This paper presents a software-based technique able to incorporate a high level of prior knowledge related to a specific object in the Computed Tomography (CT) image reconstruction process. The scanning setup evaluated in this work, which comprises a static X-ray source and a detector, allows a higher object throughput compared to conventional CT systems. However, this inline scanning geometry imposes a number of imaging constraints, which lead to smearing artefacts in the reconstructed image if conventional reconstruction techniques are used. The proposed technique can reduce those reconstruction artefacts by using distinct types of prior knowledge related to the scanned object. More precisely, the expected material density is considered by applying the Discrete Algebraic Reconstruction Technique (DART). Furthermore, the expected object shape is exploited as well by considering only the reconstruction region which lies within a specific Expected Object Domain (EOD).

**Keywords**—Inline scanning geometry; Discrete Tomography; Computed Tomography.

## I. INTRODUCTION

X-rays are widely used to analyse the internal structure of opaque objects. X-ray images, also referred to as radio-

graphs, allow the nondestructive visualization of the internal content of the object. Conventional X-ray radiography has been extensively used in inspection and quality assurance of objects [1], [2], [3]. However, one of the major disadvantages of traditional X-ray radiography is that it cannot provide quantitative 3D information about the object to be scanned. Indeed, by analyzing only a single X-ray radiograph, it is impossible to obtain depth information.

On the other hand, Computed Tomography (CT), in which multiple projections are acquired from the target object and then mathematically combined, is more suited for this purpose. Unfortunately, conventional CT systems, where the X-ray source rotates around the target object, as shown in Fig. 2, are very expensive and present a low object throughput.

The scanning setup evaluated in this work comprises a static wide cone X-ray source and a large detector for imaging objects passing by on a conveyor belt, as exposed in Fig. 3. In this scenario, the constraints associated with the imaging angular range and the number of available projections, besides the



where  $w_{ij}$  is the contribution of the  $j$ -th pixel to the  $i$ -th detector cell.

The relation between the object reconstruction  $\mathbf{v}$  and its projection  $\mathbf{p}$  can then be written as:

$$\mathbf{p} = \mathbf{W}\mathbf{v} \quad (2)$$

In *Algebraic Reconstruction Methods* (ARMs), the reconstruction problem is considered as the solving of the system of linear equations in (2). It is done by iteratively reducing the error  $\chi^2 = \|\mathbf{W}\mathbf{v} - \mathbf{p}\|^2$  along successive iterations.

#### A. Simultaneous Iterative Reconstruction Technique (SIRT)

Denoting the reconstructed object after the  $k$ -th iteration as  $\mathbf{v}^{(k)}$ , and assuming the typical initialization  $\mathbf{v}^{(0)} = 0$ , each SIRT iteration consists of three steps [11]:

- 1) Compute the forward projection of the current solution:

$$\mathbf{p}^{(k)} = \mathbf{W}\mathbf{v}^{(k)} \quad (3)$$

- 2) Compute the *residual sinogram*:

$$\mathbf{r}^{(k)} = \mathbf{p} - \mathbf{p}^{(k)} \quad (4)$$

- 3) Update the reconstruction image  $\mathbf{v}^{(k)}$  by adding a weighted backprojection of the *residual sinogram*:

$$\mathbf{v}^{(k+1)} = \mathbf{v}^{(k)} + \mathbf{C}\mathbf{W}^T\mathbf{R}\mathbf{r}^{(k)} \quad (5)$$

where  $\mathbf{R} \in \mathbb{R}^{m \times m}$  is a diagonal matrix with  $r_{ii} = 1/\sum_j w_{ij}$ . Likewise,  $\mathbf{C} \in \mathbb{R}^{n \times n}$  is a diagonal matrix with  $c_{jj} = 1/\sum_i w_{ij}$ . SIRT reconstruction process ends when a given convergence criterion is met.

#### IV. DISCRETE ALGEBRAIC RECONSTRUCTION TECHNIQUE (DART)

DART is an algebraic reconstruction method based on the interleaving of continuous update steps and discretization steps, which incorporates prior knowledge relative to the expected density of the scanned material. The flow chart of Fig. 5 shows the sequence of stages which compose the DART algorithm. Each DART stage is explained in the following:

- **Compute an initial SIRT reconstruction:** DART starts with an initial reconstruction of the acquired data  $p$  obtained with a continuous iterative reconstruction algorithm.
- **Segment the reconstruction:** the reconstruction is segmented according to the set of grey values  $(\rho_1, \rho_2, \dots, \rho_\iota)$  that is expected for the image. Since the grey values of the reconstructed image are associated with the attenuation values of the target object in each region, this incorporated prior knowledge is related to the expected density of the materials of which the object is composed. In this stage,  $\iota - 1$  thresholds  $(\tau_i)$  are applied to the image, defined as:

$$\tau_i = \frac{\rho_i + \rho_{i+1}}{2} \quad (6)$$

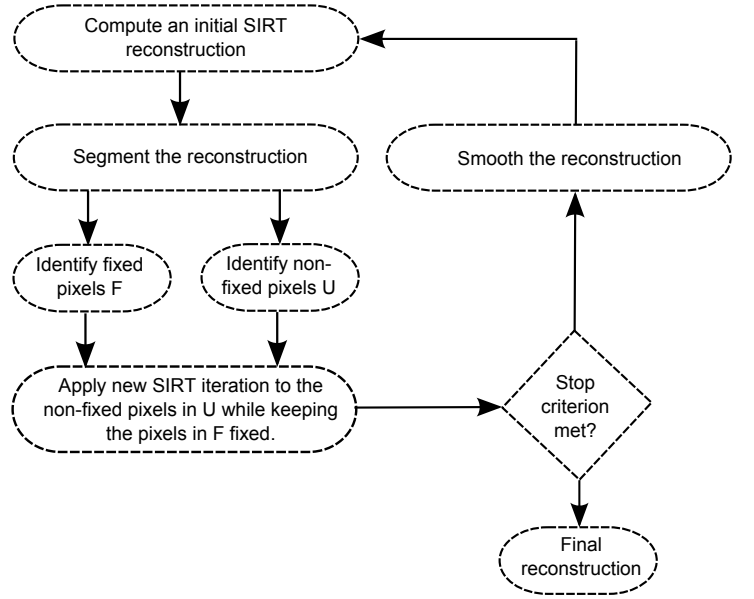


Fig. 5. Flow chart of DART algorithm.

- **Identify non-fixed pixels U:** Let  $U^{(k)} \subset \{1, 2, \dots, n\}$  be the set of pixels to be updated in the  $k$ -th iteration of DART. Since experimental results showed that SIRT leads to errors near the edges of the reconstructed image, all boundary pixels of the current segmented image are thus added to  $U^{(k)}$ . For this purpose, every pixel whose value is different from at least one of its neighbouring pixels is considered a boundary pixel. Moreover, each non-boundary pixel is added to  $U^{(k)}$  with a certain probability  $0 \leq r \leq 1$ . In this way, the accuracy of DART reconstruction is increased in case of small holes or features which were missed during the initial reconstruction.

If the prior knowledge related to the object shape is being considered, the pixels from  $U^{(k)}$  which lies outside the Expected Object Domain (EOD) are dismissed.

- **Identify fixed pixels F:** The complementary pixels set  $F^{(k)} = \{1, 2, \dots, n\} \setminus U^{(k)}$  contains all the pixels that will be removed from the reconstruction problem for the next SIRT iteration.
- **Apply new SIRT iterations to the pixels in U while keeping the pixels in F fixed:** Expanding (2), one can write:

$$\mathbf{p} = (\mathbf{w}_1 \quad \dots \quad \mathbf{w}_n) \cdot \begin{pmatrix} v_1 \\ \vdots \\ v_n \end{pmatrix} \quad (7)$$

where  $\mathbf{w}_j$  denotes the  $j$ -th column of the matrix  $\mathbf{W}$ . By removing the  $j$ -th fixed pixel from  $v$ , the reconstruction equation is updated to (8). Then, SIRT iterations are applied for this new linear system which has the same number of equations and a lower number of variables.

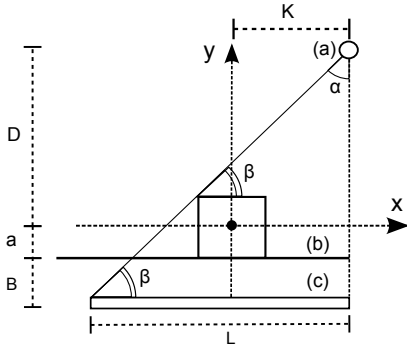


Fig. 6. Reference frame of the inline scanning geometry evaluated. The whole system is composed by a wide cone X-ray source (a), a conveyor belt (b) and a large detector (c).

TABLE I

DESCRIPTION OF THE MEASURES IN THE INLINE SCANNING GEOMETRY.

| Measure   | Description                                      |
|-----------|--|
| $D$       | distance from the object to the X-ray source     |
| $B$       | distance from the object to the detector         |
| $2a$      | size of the square which circumscribe the object |
| $2L$      | detector length                                  |
| $2\alpha$ | fanbeam opening angle                            |

$$p - w_j v_j = (w_1 \quad \cdots \quad w_{j-1} \quad w_{j+1} \quad \cdots \quad w_n) \cdot \begin{pmatrix} v_1 \\ \vdots \\ v_{j-1} \\ v_{j+1} \\ \vdots \\ v_n \end{pmatrix} \quad (8)$$

- **Stop criterion met:** The consecutive iterations of DART can be stopped according to the convergence of the total projection error or based on a fixed number of iterations.
- **Smooth the reconstruction:** Reducing the number of variables by selecting a subset of non-fixed pixels  $U^{(k)}$  may lead to more noise sensitive SIRT reconstructions. Therefore, a Gaussian smoothing filter is applied to the boundary pixels after applying the SIRT.

## V. INLINE SCANNING GEOMETRY

The experiments took place in a vectorial space centred in the scanned object, as showed in Fig. 6. The measurements  $D$ ,  $B$ ,  $a$ ,  $L$  and  $\alpha$  are defined in Table I.

The three main constraints associated with the data acquisition under this inline geometry, which bring a great challenge to the image reconstruction process, are exposed as follows:

- **Limited angular range:** due to physical limitations, the X-ray cone angle is limited to  $100^\circ$ . Thus, the object is scanned from a very limited angular views.
- **Limited number of projections:** due to the short exposure time of the radiation on the object, only a limited number of projections are acquired.

- **Truncated projections:** some projection information is lost behind the detector borders. The object is only completely imaged by the X-ray fanbeam when the distance between the object and the X-ray source is no longer than a distance  $K$ . From the Fig. 6, the value of  $K$  can be calculated as follows:

$$\tan \beta = \frac{D - a}{K + a} = \frac{D + B + a}{L} \quad (9)$$

$$K = \frac{(D - a)}{(D + B + a)} \cdot L - a \quad (10)$$

Thus, besides the very limited angular views available, the object is only fully scanned by the system when the horizontal distance to the X-ray source is smaller than  $K$ .

## VI. EXPERIMENTS

We used the ASTRA Tomography Toolbox [13] to evaluate the inline scanning geometry described in Fig. 6. Furthermore, we used different image phantoms in order to simulate scanned objects made of homogeneous materials. Fig. 7 shows cross-section slices of engine parts which were previously used in [14] (a) and in [10] (b).

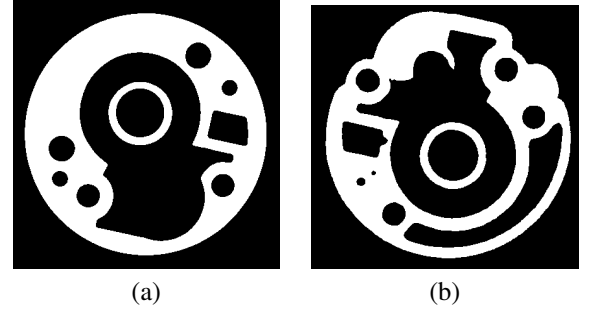


Fig. 7. Phantoms ( $512 \times 512$  pixels size) used in the experiments acquired from two parts of engines (a) [14] and (b) [10].

Fig. 8 (a) shows a phantom generated from an image of a cross-section slice of cheese (b). It is a real challenge to obtain the reconstruction accuracy necessary to study the hole size distribution in this phantom having in mind the constraints imposed by the inline scanning geometry.

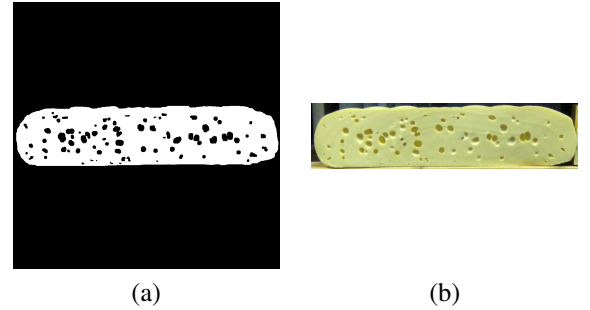


Fig. 8. Phantom ( $512 \times 512$  pixels size) of a cross-section slice of cheese (a) generated from a real image (b).

## VII. RESULTS

Fig. 9, 10, and 11 show the reconstruction results obtained in simulation experiments using the phantoms shown in Fig. 7 (a), (b) and Fig. 8 (a), respectively, using a fanbeam opening angle ( $2\alpha$ ) of  $100^\circ$ .

DART algorithm was configured to run 100 SIRT iterations to built an initial reconstruction, and then each new DART iteration comprised 10 SIRT iterations. This way, after running 510 SIRT iterations, for example, the DART algorithm performed 41 iterations. The images along a same line on Fig. 9, 10, and 11 show the obtained reconstructions after 110, 1100 and 6100 SIRT iterations, respectively. In a column, the results of distinct reconstruction techniques are exposed. The S-SIRT method is a conventional SIRT reconstruction followed by an image segmentation using the Otsu's method [15].

Prior knowledge on the object shape was exploited in the experiments by restricting the available reconstruction area to the voxels belonging to the EOD (highlighted in red lines).

Fig. 12, 13 and 14 show the decrease of the number of misclassified pixels in the reconstructions of phantoms shown in Fig. 7 (a), (b) and Fig. 8 (a), respectively, as a function of the number of the algorithm iterations.

## VIII. CONCLUSION

The obtained results show a significant improvement in the reconstruction quality when prior knowledge related to the scanned object is considered. More specifically, when prior knowledge on the expected density of the material is combined with the expected shape of the object. The presented software based technique is able to overcome the low amount of acquired data in the inline X-ray geometry due the constraints imposed by the limited angular imaging range.

## REFERENCES

- [1] R. Eilbert and S. Shi, "Improved imaging for x-ray inspection systems," *Aerospace and Electronic Systems Magazine, IEEE*, vol. 20, no. 3, pp. 23–28, March 2005.
- [2] B. Pierce, D. Shelton, H. Longbotham, S. Baddipudi, and P. Yan, "Automated inspection of through hole solder joints utilizing x-ray imaging," *Aerospace and Electronic Systems Magazine, IEEE*, vol. 9, no. 2, pp. 28–32, Feb 1994.
- [3] Z. Tong, T. Liao, and C. Strittmatter, "Automated x-ray inspection of chip-to-chip interconnections of si-on-si mcm's," *Components, Packaging, and Manufacturing Technology, Part B: Advanced Packaging, IEEE Transactions on*, vol. 18, no. 4, pp. 666–674, Nov 1995.
- [4] K. J. Batenburg and J. Sijbers, "DART: a practical reconstruction algorithm for discrete tomography," *IEEE Transactions on Image Processing*, vol. 20, no. 9, pp. 2542–53, Sep. 2011.
- [5] G. Van Gompel, K. Batenburg, E. Van de Castele, W. Van Aarle, and J. Sijbers, "A discrete tomography approach for superresolution micro-ct images: application to bone," in *Biomedical Imaging: From Nano to Macro, 2010 IEEE International Symposium on*, April 2010, pp. 816–819.
- [6] K. Batenburg and J. Sijbers, "Discrete tomography from micro-ct data: application to the mouse trabecular bone structure," in *Medical Imaging. International Society for Optics and Photonics, 2006*, pp. 614240–614240.
- [7] K. J. Batenburg, S. Bals, J. Sijbers, C. Kübel, P. A. Midgley, J. C. Hernandez, U. Kaiser, E. R. Encina, E. a. Coronado, and G. Van Tendeloo, "3D imaging of nanomaterials by discrete tomography," *Ultramicroscopy*, vol. 109, no. 6, pp. 730–40, May 2009.

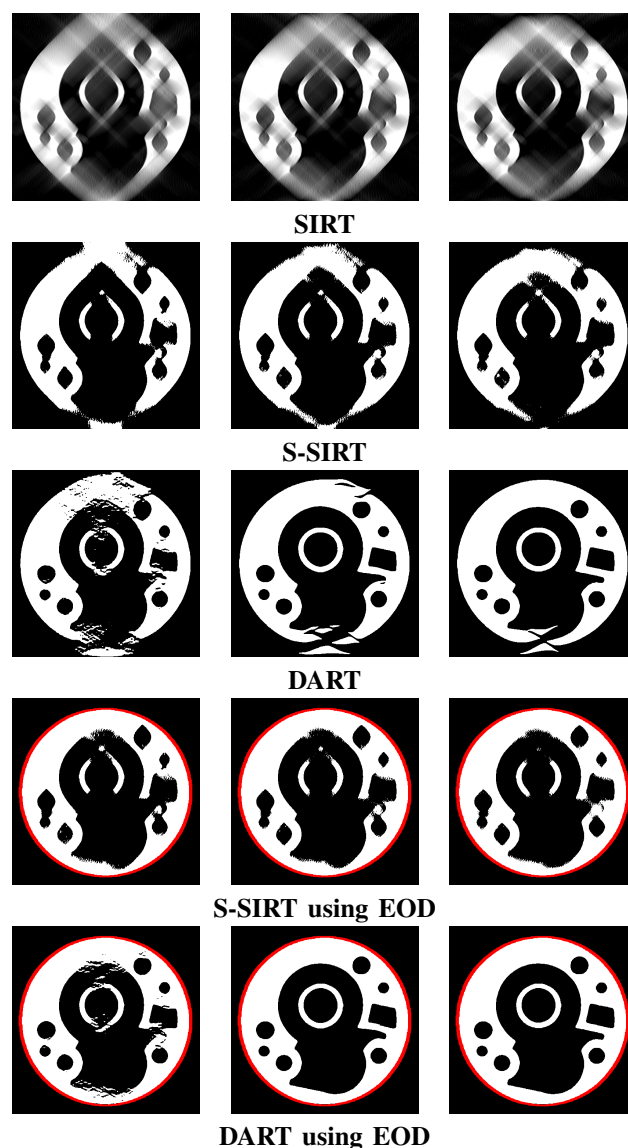


Fig. 9. The images along a same line show the obtained reconstructions, of phantom Fig. 7 (a), after 110, 1100 and 6100 SIRT iterations, respectively. Along a same column, the image results of distinct reconstruction techniques are exposed.

- [8] K. J. Batenburg, J. Sijbers, H. F. Poulsen, and E. Knudsen, "DART : A Robust Algorithm for Fast Reconstruction of 3D Grain Maps," *Journal of Applied Crystallography*, vol. 43, pp. 1464–1473, 2010.
- [9] D. Brasse, B. Humbert, C. Mathelin, M.-C. Rio, and J.-L. Guyonnet, "Towards an inline reconstruction architecture for micro-ct systems," *Physics in Medicine and Biology*, vol. 50, no. 24, p. 5799, 2005.
- [10] S. Oeckl, T. Wenzel, S. Gondrom, and F. Rauch, "Real inline x-ray 3d ct with short cycle times for light metal casting inspection in production," *Nuclear Science Symposium Conference Record, 2008. NSS '08. IEEE*, pp. 562–564, Oct 2008.
- [11] J. Gregor and T. Benson, "Computational analysis and improvement of sirt," *Medical Imaging, IEEE Transactions on*, vol. 27, no. 7, pp. 918–924, 2008.
- [12] T. M. Buzug, *Computed tomography: from photon statistics to modern cone-beam CT*. Springer, 2008.
- [13] W. J. Palenstijn, K. J. Batenburg, and J. Sijbers, "Performance improvements for iterative electron tomography reconstruction using graphics processing units (gpus)," *Journal of Structural Biology*, vol. 176, pp. 250–253, 2011.

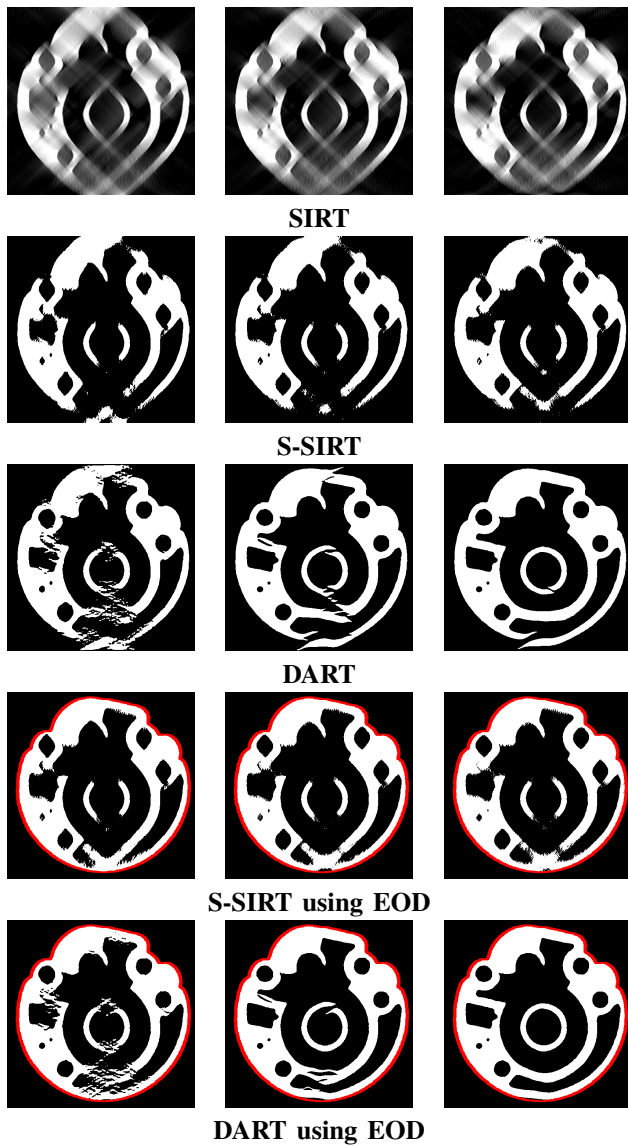


Fig. 10. The images along a same line show the obtained reconstructions, of phantom Fig. 7 (b), after 110, 1100 and 6100 SIRT iterations, respectively. Along a same column, the image results of distinct reconstruction techniques are exposed.

[14] T. Fuchs, T. Wenzel, and I. Bauscher, "Fast inline computed tomography in industrial non-destructive testing," *Development Center X-ray technology (EZRT); Fraunhofer Institute for Integrated Circuits (IIS), Frth, Germany*.

[15] N. Otsu, "A threshold selection method from gray-level histograms," *Automatica*, vol. 11, no. 285-296, pp. 23-27, 1975.

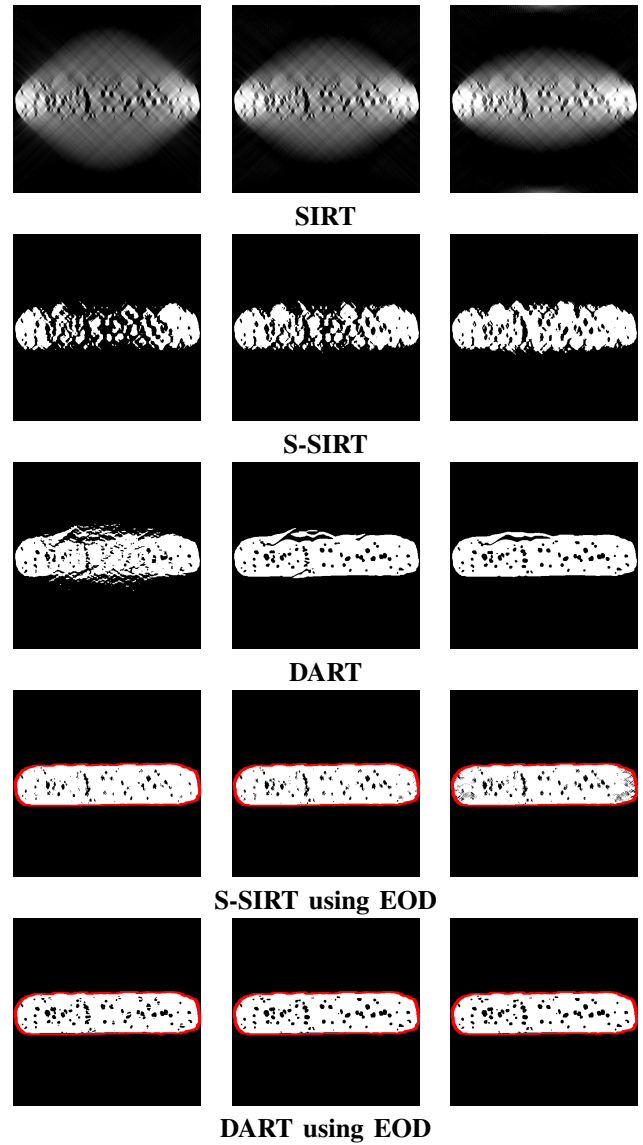


Fig. 11. The images along a same line show the obtained reconstructions, of phantom Fig. 8 (a), after 110, 1100 and 6100 SIRT iterations, respectively. Along a same column, the image results of distinct reconstruction techniques are exposed.

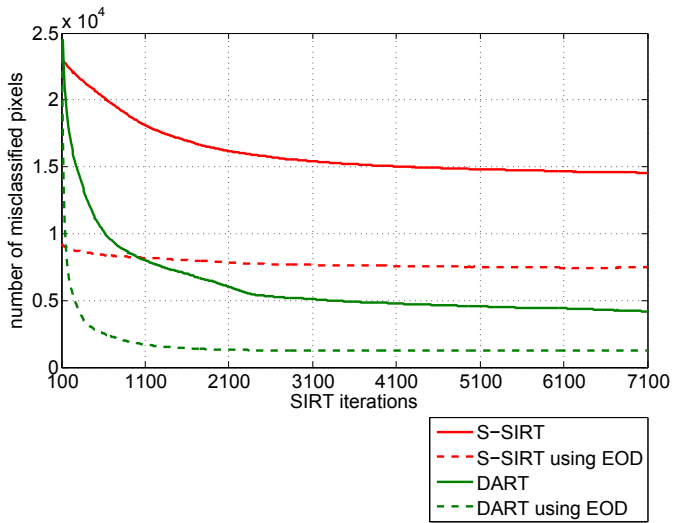


Fig. 12. The number of misclassified pixels for the reconstructions of the phantom shown in Fig. 7 (a) as a function of the number of iterations for the evaluated algorithms in the inline X-ray geometry.

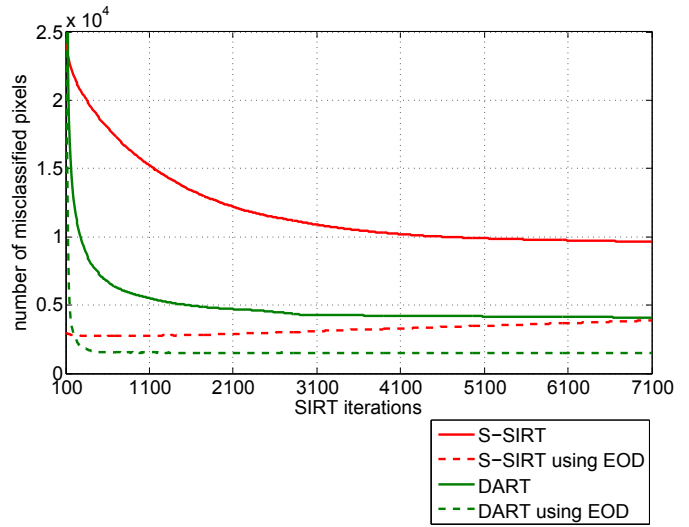


Fig. 14. The number of misclassified pixels for the reconstructions of the phantom shown in Fig. 8 (a) as a function of the number of iterations for the evaluated algorithms in the inline X-ray geometry.

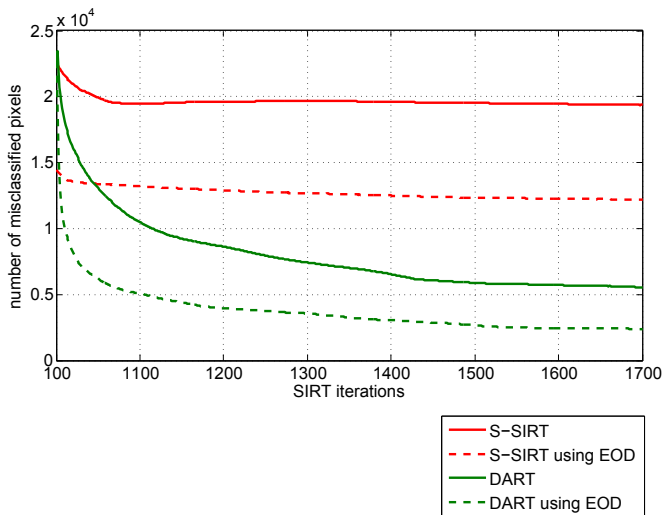


Fig. 13. The number of misclassified pixels for the reconstructions of the phantom shown in Fig. 7 (b) as a function of the number of iterations for the evaluated algorithms in the inline X-ray geometry.